

ARMY RESEARCH LABORATORY



Use of Self-Propagating High-Temperature Synthesis Reactions in Refractory Alloy Fabrication

by Laszlo J. Kecske

ARL-TR-3465

April 2005

NOTICES

Disclaimers

The findings in this report are not to be construed as an official Department of the Army position unless so designated by other authorized documents.

Citation of manufacturer's or trade names does not constitute an official endorsement or approval of the use thereof.

Destroy this report when it is no longer needed. Do not return it to the originator.

Army Research Laboratory

Aberdeen Proving Ground, MD 21005-5069

ARL-TR-3465

April 2005

Use of Self-Propagating High-Temperature Synthesis Reactions in Refractory Alloy Fabrication

**Laszlo J. Kecske
Weapons and Materials Research Directorate, ARL**

REPORT DOCUMENTATION PAGE				Form Approved OMB No. 0704-0188	
<p>Public reporting burden for this collection of information is estimated to average 1 hour per response, including the time for reviewing instructions, searching existing data sources, gathering and maintaining the data needed, and completing and reviewing the collection information. Send comments regarding this burden estimate or any other aspect of this collection of information, including suggestions for reducing the burden, to Department of Defense, Washington Headquarters Services, Directorate for Information Operations and Reports (0704-0188), 1215 Jefferson Davis Highway, Suite 1204, Arlington, VA 22202-4302. Respondents should be aware that notwithstanding any other provision of law, no person shall be subject to any penalty for failing to comply with a collection of information if it does not display a currently valid OMB control number.</p> <p>PLEASE DO NOT RETURN YOUR FORM TO THE ABOVE ADDRESS.</p>					
1. REPORT DATE (DD-MM-YYYY)	2. REPORT TYPE			3. DATES COVERED (From - To)	
April 2005	Final			January 1994–December 1999	
4. TITLE AND SUBTITLE				5a. CONTRACT NUMBER	
Use of Self-Propagating High-Temperature Synthesis Reactions in Refractory Alloy Fabrication				5b. GRANT NUMBER	
				5c. PROGRAM ELEMENT NUMBER	
				5d. PROJECT NUMBER	
				1L622105AH84-622195A	
				5e. TASK NUMBER	
				5f. WORK UNIT NUMBER	
7. PERFORMING ORGANIZATION NAME(S) AND ADDRESS(ES)				8. PERFORMING ORGANIZATION REPORT NUMBER	
U.S. Army Research Laboratory ATTN: AMSRD-ARL-WM-MD Aberdeen Proving Ground, MD 21005-5069				ARL-TR-3465	
9. SPONSORING/MONITORING AGENCY NAME(S) AND ADDRESS(ES)				10. SPONSOR/MONITOR'S ACRONYM(S)	
				11. SPONSOR/MONITOR'S REPORT NUMBER(S)	
12. DISTRIBUTION/AVAILABILITY STATEMENT					
Approved for public release; distribution is unlimited.					
13. SUPPLEMENTARY NOTES					
14. ABSTRACT					
<p>The titanium carbide (TiC) self-propagating high-temperature synthesis (SHS) reaction was used in a hot-explosive-consolidation process to fabricate tungsten and molybdenum-based alloy billets. In this method, a Ti+C mixture is reacted to provide a source of heat for the refractory precursor powders. As the TiC reaction proceeds, the exterior of the alloy sample heats up rapidly, near or above 2000 °C, while its interior lags behind, heating up more gradually to 1600 °C. At the completion of the TiC reaction, the alloy sample's exterior begins to cool, causing the temperature to equilibrate to an isothermal condition. At this time, the sample is compacted to high density by the application of an explosively generated pressure wave. Experiments were conducted to determine the relationship between the geometries of the Ti+C mixture and the alloy sample. For the Ti+C mixture, a doughnut arrangement was found to provide an optimum heating rate and temperature profile to the sample. The effects of the relative amount of the SHS material and alloy sample on the duration of the heating cycle, peak interior temperature, and rate of cooling were studied. The properties of the samples and TiC product were evaluated by density measurements, scanning electron microscopy, energy-dispersive x-ray spectroscopy, and x-ray diffraction analysis. The HEC method and the resultant product structures are described.</p>					
15. SUBJECT TERMS					
explosive compaction, refractory alloys, processing, microstructure, tungsten, molybdenum, titanium					
16. SECURITY CLASSIFICATION OF:			17. LIMITATION OF ABSTRACT	18. NUMBER OF PAGES	19a. NAME OF RESPONSIBLE PERSON
a. REPORT UNCLASSIFIED	b. ABSTRACT UNCLASSIFIED	c. THIS PAGE UNCLASSIFIED			Laszlo J. Kecske
			UL	26	19b. TELEPHONE NUMBER (Include area code) 410-306-0811

Contents

List of Figures	iv
1. Introduction	1
2. Experimental Procedures	2
2.1 Heat-Balance Calculations	2
2.2 Temperature Measurements	2
2.3 Compaction Experiments	4
3. Results and Discussion	5
3.1 Temperature Measurements	5
3.2 Compaction Characteristics.....	10
3.3 Alloy Substructures	13
4. Conclusions	16
5. References	17
Distribution List	19

List of Figures

Figure 1. Schematic diagram of the fixture used in the temperature measurements.	3
Figure 2. Schematic diagram of the HEC fixture.	4
Figure 3. Temperature data for W–Ti; $n_{TiC}/n_s = 3.2$	7
Figure 4. Temperature data for W–Ti; $n_{TiC}/n_s = 6.3$	7
Figure 5. Temperature data for W–Ti; $n_{TiC}/n_s = 9.1$	8
Figure 6. Interior temperature data for W–Ti; $n_{TiC}/n_s = 3.2$, $n_{TiC}/n_s = 6.3$, and $n_{TiC}/n_s = 9.1$ is shown in 3-D.....	8
Figure 7. Temperature data for Mo–Ti; $n_{TiC}/n_s = 5.8$	10
Figure 8. Temperature data for W–Ti in the scaled-up fixture; $n_{TiC}/n_s = 6.0$	11
Figure 9. Macrophotographs of a typical W–Ti billet showing top, bottom, and side views (sectioned billet placed bottom to bottom).....	12
Figure 10. XRD scans of typical HEC billet core regions; W–Ti is shown in 7A and Mo–Ti is shown in 7B.....	13
Figure 11. XRD scans of typical HEC billet core regions; W Ti is shown in 7A and Mo Ti is shown in 7B.....	14
Figure 12. SEMs of polished surfaces of typical HEC billet core regions; W–Ti is shown in 8A and Mo–Ti is shown in 8B.....	15

1. Introduction

Traditional forming routes of melting, casting, and forging are usually unsuitable for the preparation and processing of refractory-metal-based multiphase alloys. Often, when the extent of intermixing of the constituents is to be severely restricted, nonconventional powder metallurgy (PM) fabrication techniques, such as the use of high explosives for consolidation, may be sought out. PM is also more practical since near-net-shape products significantly reduce the need for machining.

Explosive compaction is attractive because the rapid passage of a shock wave through the powder bed generates very high pressures and, therefore, frictional heating and melting occurs between adjacent particles. As such, intergrain bonding is produced on a microscopic level. The ease of compaction is strongly related to the nature of the powder assemblage, its particle size, size distribution, shape, and packing density. Due to the rapid densification rate, dynamically consolidated samples often suffer from low densities, poor bonding, and cracking (1). High-detonation-velocity explosives (6000–8000 m/s) can produce the desired hardness, intergrain bonding, and compressive strength, however, with profuse cracking. Cracking may be reduced by using low-detonation-velocity explosives (2000–4000 m/s), but at the expense of consolidation quality.

Conventional hot-explosive-consolidation (HEC) has been suggested as a way to reduce structural integrity problems (2, 3). In HEC, the powder mixture is sealed in a container, heated in a furnace, quickly removed, transferred into the compaction fixture, and consolidated. The primary advantage of heating is to decrease the material's yield strength, thereby increasing its ductility. In recent years, several research groups (4–10) have explored HEC.

To limit the intermixing of components that would occur during long heating times in a furnace, a modified HEC method was developed. This technique uses an in-situ titanium carbide (TiC) “chemical furnace” to heat the powder sample prior to compaction (10). In-situ heating also reduces the complexity of the assembly since the precursors are now heated and consolidated in the same fixture.

The idea of “chemical heating” first appeared in conjunction with hot-working of metals (11). Since then, others have also attempted to shock-initiate admixed exothermic mixtures to locally enhance sample properties (5, 8, 12).

The chemical furnace is simply an exothermic powder mixture of reactants that, when allowed to react, generates heat yielding high temperatures. Such reactions are a subclass of combustion synthesis or self-propagating high-temperature synthesis (SHS) reactions (13–15). In SHS, the products are directly synthesized from their elemental precursors, via the propagation of a solid-solid combustion front through a green powder compact (e.g., $Ti + C \rightarrow TiC$). Once the process is initiated, the heat of reaction sustains the reaction until all of the reactants have been consumed. These reactions are characterized by rapid reaction rates (~1 cm/s), temperatures over 3000 °C, and

the evolution of trapped impurities from the reactants. Potential advantages of the combustion synthesis process are that it requires little energy input and the processing time is reduced from hours to seconds.

The primary objective of this effort was to examine the feasibility of scaling up the HEC process with the use of SHS reactions to fabricate high-density, two-phase tungsten-titanium (W–Ti) and molybdenum titanium (Mo–Ti) alloys. This required the examination of several processing parameters. Since the SHS reaction heating cycle is inherently short, a critical advantage of this technique would be the retention of desirable precursor properties, such as grain size distribution and morphology. Then, if possible, successful adjustments of the available heat and peak temperature achieved during heating would limit the extent of sintering, dissolution, and melting in each component. Therefore, the effects of sample configuration and the molar ratio of sample and chemical furnace on the structural evolution of the product were of primary concern.

The test program was carried out in several steps, starting with baseline calculations to identify the amount of TiC needed to heat the alloy samples. After a series of auxiliary temperature measurements were performed, to experimentally validate the baseline computations, accurately determine the peak temperatures and heating times in the fixture, several W–Ti and Mo–Ti alloy billets were fabricated. Finally, the HEC process, designed for 5-cm-diameter, 1-cm-thick billets, was scaled up to fabricate 7.5-cm-diameter, 1-cm-thick W–Ti billets.

2. Experimental Procedures

2.1 Heat-Balance Calculations

Adiabatic heat-balance computations were performed for each of the sample systems to determine the required amount of chemical furnace (i.e., a baseline value). Briefly, in the calculations, the exothermic heat of formation of TiC (heat output) was equated to the heat required by the sample powder mixture (heat input) to elevate its temperature a known amount. Heat inputs for contributions from phase transitions (e.g., α -Ti \rightarrow β -Ti) were included. However, the calculations did not consider heat losses or geometrical constraints in the reaction-compaction fixture. Results indicated that a ratio of moles of TiC to moles of sample (n_{TiC}/n_s) of 1.0 would cause the Ti component to melt.

2.2 Temperature Measurements

High-purity (99.9%) 12- μ m W (Johnson Matthey, Ward Hill, MA), 99.9%-pure –325-mesh (equivalent to –44 μ m) Mo (CERAC Inc., Milwaukee, WI), and 99.5%-pure –325-mesh Ti (Micron Metals, Gates City, UT) were used for the fabrication of the HEC alloy samples. Also, 99.5%-pure –325-mesh Ti (Micron Metals, Gates City, UT) and 99.9%-pure 2- μ m graphite (C) (CERAC Inc., Milwaukee, WI) were used for the TiC chemical furnace.

The W and Ti or Mo and Ti powder mixtures were ball-milled for at least 6 hr under an argon (Ar) atmosphere. The W:Ti ratio was 83:17 atomic percent (a/o) in all of the W–Ti alloys, and the Mo:Ti ratio was 82:18 a/o in the Mo–Ti alloy. A Ti:C molar ratio of 1.0 was maintained in all of the Ti and C powder mixtures. The Ti and C powders were also dry-mixed and ball-milled under Ar atmosphere. The Ti+C powder mixture was pressed at 44 MPa into 100-mm-outer-diameter, 50-mm-inner-diameter, and 20-mm-thick doughnut-shaped green compacts.

The auxiliary experiments were carried out with respect to the ratio of moles of TiC exothermic material to moles of alloy sample (n_{TiC}/n_s) to measure the sample temperature and rate of heating in the reaction-compaction fixture during the heating phase of the HEC process. For these measurements, the explosive container was not used. Instead, a series of five W–5Re/W–26Re thermocouples were inserted through the base of the reaction vessel into the middle of the powder sample. Two chromel-alumel thermocouples were also placed in the vessel, one near the electric match and another beneath the Ti+C doughnut, to mark the start and end of the TiC reaction. Figure 1 depicts the block diagram of the fixture with the lateral arrangement of the thermocouples. In these experiments, once the SHS reaction was initiated, the electro motive force (EMF) output of the thermocouples was recorded as a function of time.

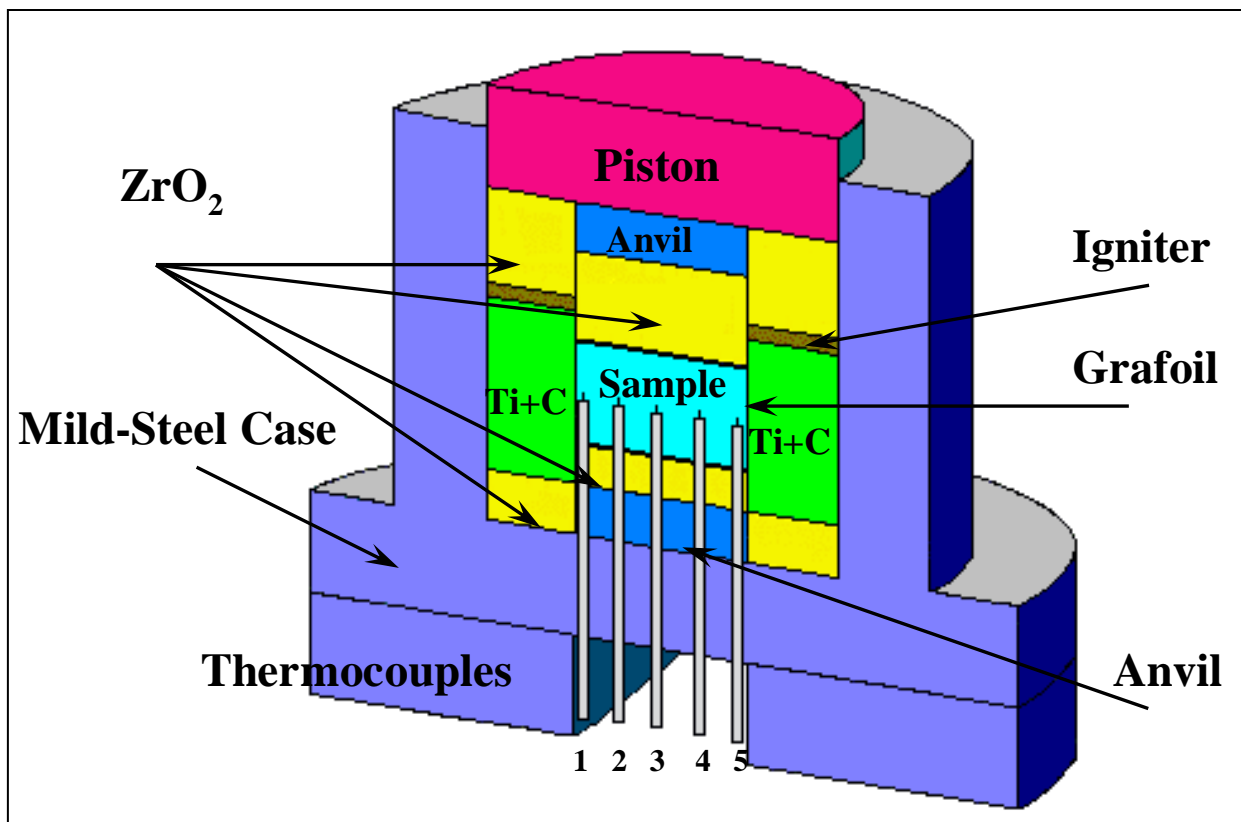


Figure 1. Schematic diagram of the fixture used in the temperature measurements.

Several separate temperature-time measurements were made. In the first series for W–Ti, the n_{TiC}/n_s values were set to 3.2, 6.3, or 9.1. In the fourth measurement for Mo–Ti, the n_{TiC}/n_s was

5.9. Another measurement was made in the scale-up fixture. In the scale-up fixture, the overall lateral dimensions of the TiC chemical furnace and alloy sample were scaled up by a factor of 1.5, while the vertical dimensions remained unchanged. The scale-up measurement was with W-Ti, using a n_{TiC}/n_s of 6.0.

2.3 Compaction Experiments

Figure 2 shows the schematic of the HEC reaction vessel. The vessel was designed to contain the Ti+C SHS reaction and, at the same time, to serve as the explosive compaction fixture. The lid assembly of the vessel was fitted with a container that held the explosive charge. The mild-steel vessel contained the alloy powder sample, the Ti+C green compact, zirconia (ZrO_2), graphite sheet insulation, igniter mixture, electric igniter (not shown), and the explosive driver package. The explosive driver package consisted of a set of high-hardness steel anvils, aluminum piston (lid assembly), poly vinyl chloride (PVC) container holding powdered Amatol (80:20 NH_4NO_3 :TNT) explosive (detonation velocity = 3850 m/s), detasheet booster, and the detonator.

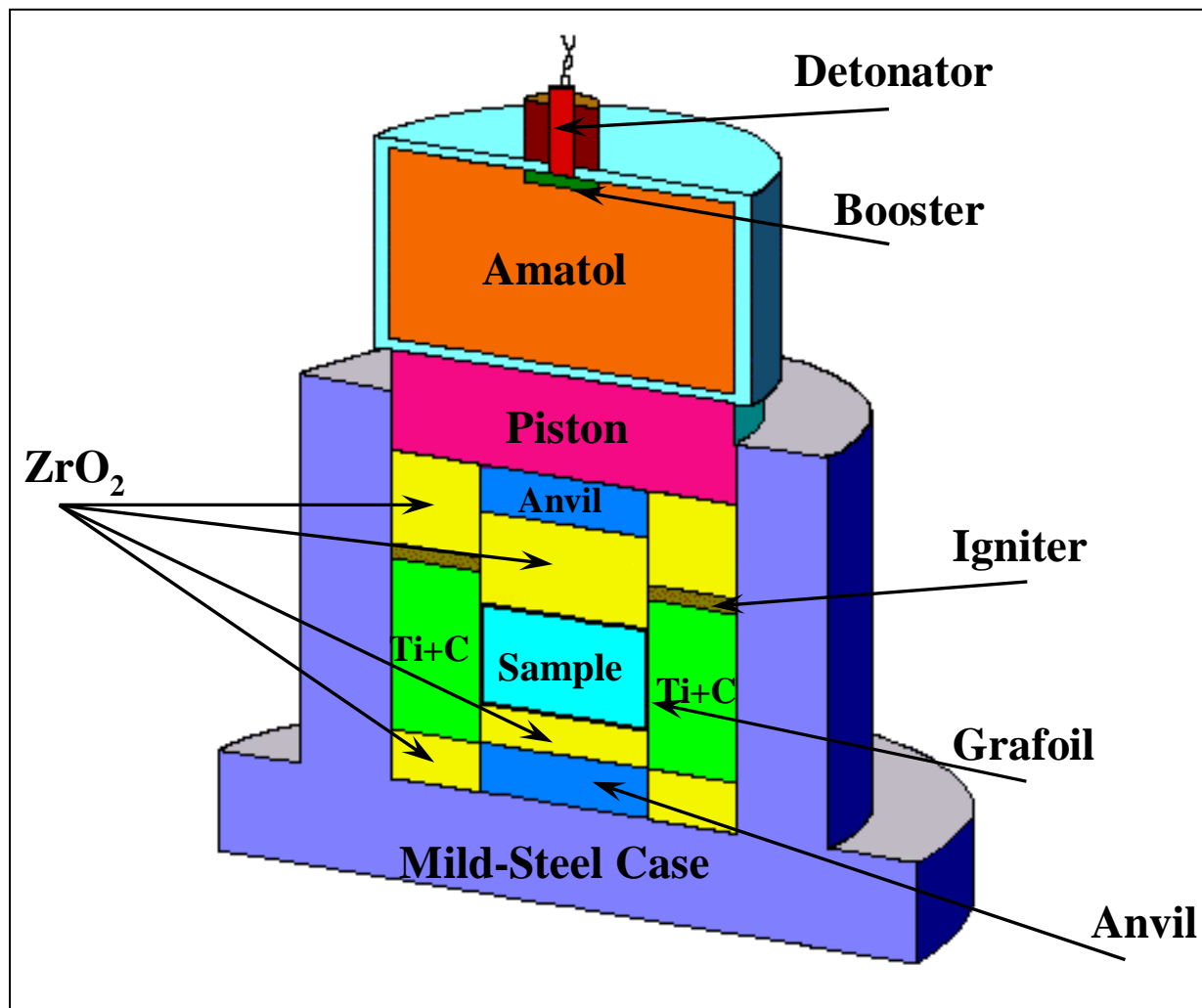


Figure 2. Schematic diagram of the HEC fixture.

Because large quantities of volatile impurities are released by the TiC SHS reaction, vent holes were drilled into the mild-steel vessel. ZrO_2 was used to limit heat losses from the reacting Ti+C compact and to protect the piston assembly and explosives from overheating. The graphite sheet functioned as an inert barrier, preventing the diffusion of contaminants into the sample.

Commercial model-rocket igniters were used to initiate the SHS reaction. The electric match was remotely activated, which, in turn, initiated the igniter mixture and Ti+C green compact. As the TiC reaction proceeded to completion, normally in about 3 s, the alloy powder sample was heated (via diffusion) to high temperatures. When the optimum amount of time had elapsed, the piston, accelerated by the detonation of the explosive, densified both the sample and the TiC doughnut. When the fixture and its contents cooled to ambient temperature, the sample billet was extracted.

After the extraction of the billet, the typical postconsolidation characterization of the samples consisted of macrophotography, sectioning, determination of the bulk density, and metallographic preparation of scanning electron microscopy (SEM), energy-dispersing x-ray spectroscopy (EDS), and x-ray diffraction analysis (XRD) samples. The compaction uniformity of the billets was evaluated by density measurements. The billets were cut into several roughly equal sections, and the mass density was measured with a water immersion technique. The measurements revealed that the billets were uniformly dense with a variation of about $\pm 0.5\%$. The billets were further sectioned into wafers (parallel or perpendicular to the compaction direction) for SEM, EDS, and XRD. Each XRD sample was polished and mounted into sample holders, then step-scanned through a 2θ range of 20 – 120° using a 0.025° increment and a 5-s dwell time. SEM, EDS, and XRD were also used to examine the precursor powders. It may be noted that the graphite was not analyzed beyond SEM.

Three W–Ti billets were produced, using an explosive charge mass to piston mass ratio (c/m) of 1.7 ± 0.1 . The n_{TiC}/n_s values were 3.2, 6.4, or 8.3. Note the slight deviation from the n_{TiC}/n_s values used in the temperature measurements. The c/m value of ~ 1.7 was found to produce samples with optimum (i.e., highest density without excessive cracking) results. For the W–Ti billet that was made in the scale up fixture, the c/m was 2.0 and the n_{TiC}/n_s was 6.4. Finally, an Mo–Ti billet was consolidated with a c/m of 2.1 and n_{TiC}/n_s of 5.8.

3. Results and Discussion

Preliminary configurational experiments determined that placement of the TiC chemical furnace in a concentric geometry is most suitable for uniform consolidation. Compactions using layered (e.g., sandwich) and complete envelopment geometries did not achieve simultaneous ignition of separated chemical furnace elements, resulting in nonuniform compactions and sample densities. Sample billets also tended to contain large radial and laminar macrofractures.

3.1 Temperature Measurements

The results of the measurements of the precursor-powder-bed temperature during the heating phase were essential for the consolidation of the alloy billets. The experiments revealed the peak

temperatures and thermal gradients within the sample powder bed and also indicated the optimum time for consolidation. The results also showed that there were significant heat losses in the HEC fixture.

The data for W–Ti corresponding to n_{TiC}/n_s values of 3.2, 6.3, and 9.1 are presented in figures 3–5. In the lower left-hand corner of figures 3–5, the pair of vertical arrows marks the duration of the TiC reaction. (Note, in figures 3 and 5, the second arrows are partially masked by the thermocouple trace.) The temperature-time trace at the center of the powder bed (TC no. 3) for each case is shown on an expanded scale in figure 6. As expected, with an increasing amount of TiC, the duration of the SHS reaction increases. In all three cases, the temperature at the edge of the powder beds rises rapidly to reach a broad peak; drops; goes through a plateau; then, due to continued heat losses, steadily decreases. As the heat diffuses inward to the sample center, the temperature profile is changed. At the center, a more sluggish rise in the temperature and the absence of the short-term peak result in a wider plateau and subsequent decline only. Thus, an immediate conclusion from the data is that the periphery of the powder bed undergoes a different thermal history than the midregions.

For $n_{TiC}/n_s = 3.2$, the peak temperature is 1500 °C at one edge and is near the melting point of Ti at the other (T_m Ti = 1670 °C). The center reaches only 1250 °C, well below T_m Ti. Whereas, for $n_{TiC}/n_s = 6.3$, the edge temperature reaches 1900 °C at one end and 2100 °C at the other. In this case, the center temperature is higher, reaching 1550 °C, but does not exceed T_m Ti. Finally, for $n_{TiC}/n_s = 9.1$, the powder bed reaches temperatures above 2400 °C at its periphery and 1650 °C at its center. The heating rates for n_{TiC}/n_s values of 3.2 and 6.3 are similar, but, for $n_{TiC}/n_s = 9.1$, it is different. Specifically, the temperature rise at the center is more rapid, much like that of the periphery. With n_{TiC}/n_s values of 6.3 and 9.1, the critical aspect of the data is that at about 60 s after the initiation of the TiC reaction, the entire W+Ti powder bed becomes effectively isothermal. For $n_{TiC}/n_s = 3.2$, the interior of the powder bed does not reach an isothermal plateau at 60 s and is subject to moderate temperature gradients. Only considerably later (over 120 s; not shown) at a much lower temperature, during overall cooling, is thermal equilibrium reached.

Differences of the temperature profiles are primarily due to the amount of TiC furnace and slight changes with n_{TiC}/n_s of the TiC doughnut/sample geometry. The packing density ratio of the TiC furnace and sample is ~3. As a result, the respective volumes of the chemical furnace and the sample are roughly the same for $n_{TiC}/n_s = 3.2$. Whereas, the volume of TiC is twice that of the sample for $n_{TiC}/n_s = 6.3$ and three times that of the sample for $n_{TiC}/n_s = 9.1$. Therefore, the TiC doughnut completely encloses for $n_{TiC}/n_s = 9.1$, and partially encloses for $n_{TiC}/n_s = 6.3$, the ZrO_2 insulation above and beneath the sample. Then, as the TiC reacts, the ZrO_2 is also heated. The hotter insulation, in turn, provides greater heating to the sample, resulting in a faster internal temperature rise. However, for $n_{TiC}/n_s = 3.2$, most of the ZrO_2 lies outside of the TiC doughnut. Without direct heat from the TiC reaction, the ZrO_2 acts as a heat sink, lessening the interior temperature rise.

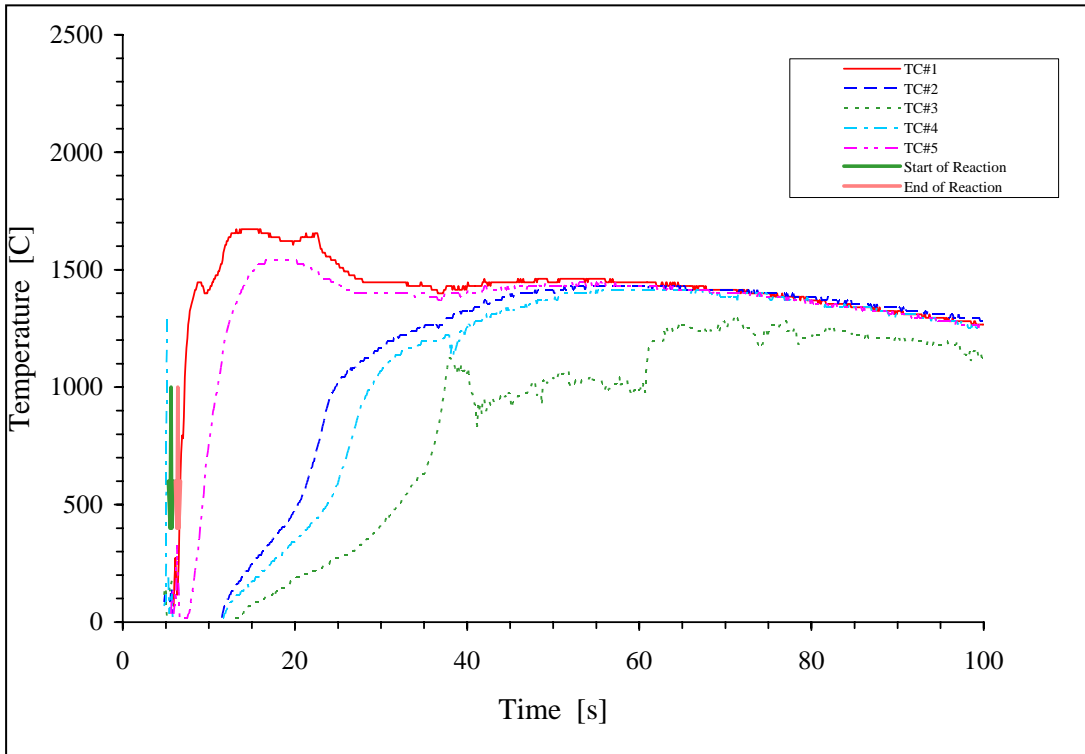


Figure 3. Temperature data for W-Ti; $n_{\text{TiC}}/n_s = 3.2$.

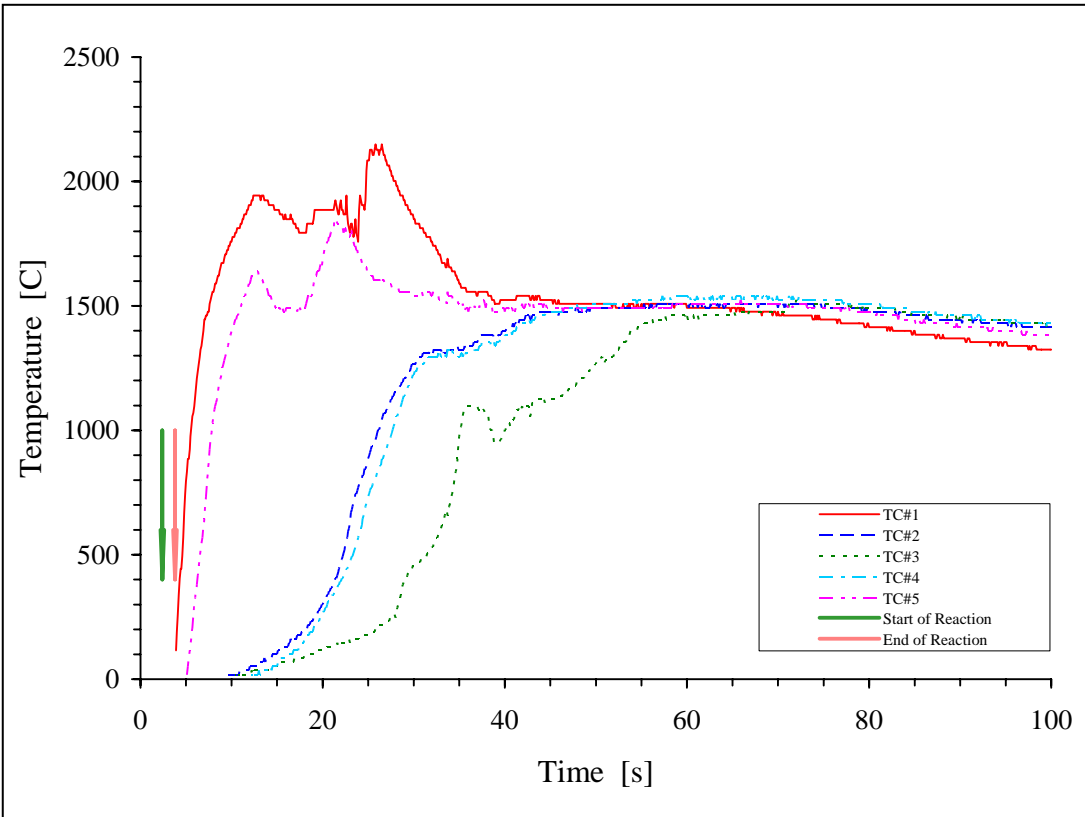


Figure 4. Temperature data for W-Ti; $n_{\text{TiC}}/n_s = 6.3$.

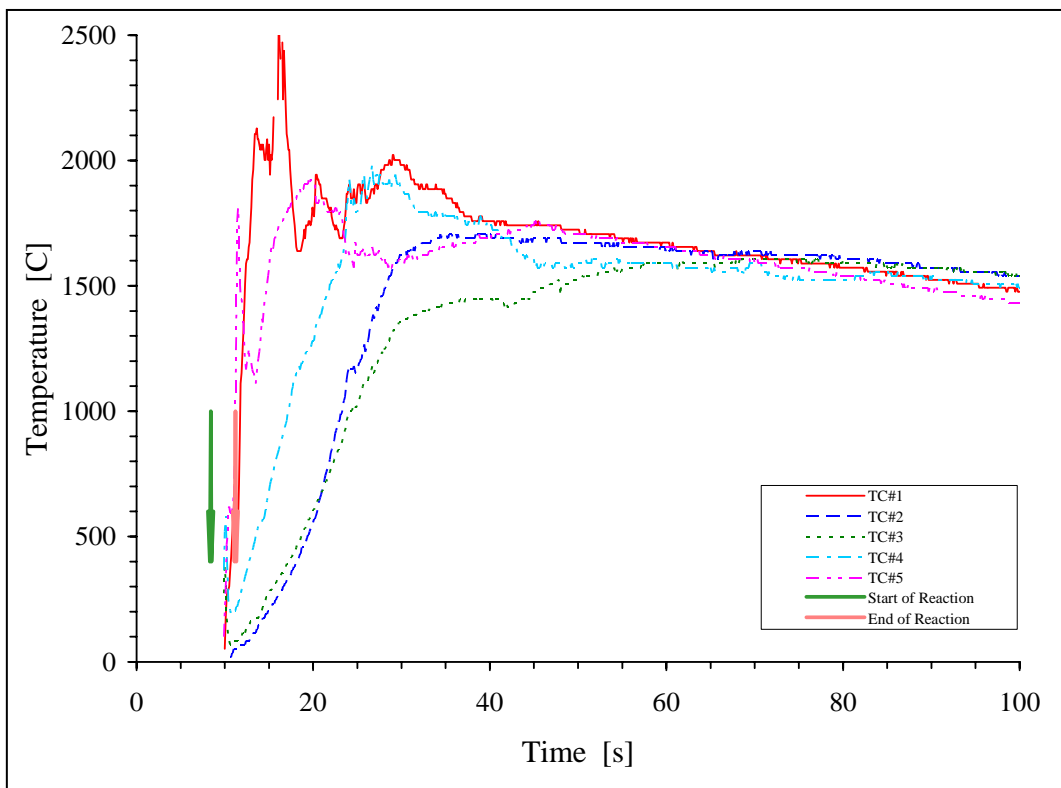


Figure 5. Temperature data for W-Ti; $n_{\text{TiC}}/n_s = 9.1$.

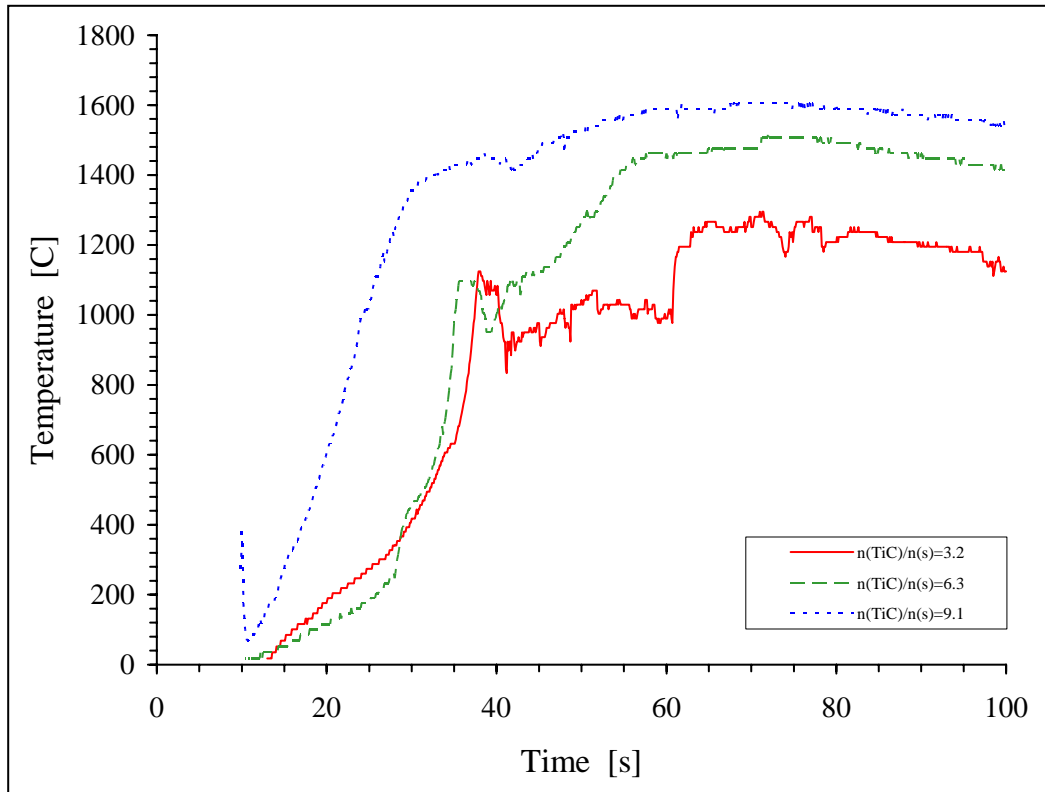


Figure 6. Interior temperature data for W-Ti; $n_{\text{TiC}}/n_s = 3.2$, $n_{\text{TiC}}/n_s = 6.3$, and $n_{\text{TiC}}/n_s = 9.1$ is shown in 3-D.

The profile of the center thermocouple in figure 3 ($n_{TiC}/n_s = 3.2$) is also noisier, and it exhibits a 150–200 °C temperature drop lasting for about 20 s. After this temporary heat loss, the temperature continues to rise. The center thermocouple profile in figure 4 ($n_{TiC}/n_s = 6.3$) reflects a similar behavior, but the effect is less pronounced. The increased temperature fluctuation and/or decrease (heat loss) are probably attributed to a partial failure (cracking and delamination) of the ZrO_2 insulation beneath the sample powder bed. The insulation is cooler for the smaller n_{TiC}/n_s value; a cooler ZrO_2 may be more prone to greater thermal gradients that would likely generate higher internal stresses and cause cracking. Such cracks that disrupt the integrity of the thermally insulating barrier could possibly account for the observed temperature fluctuations and/or drops.

The data in figures 3–6 reveal that the n_{TiC}/n_s significantly affects the heating rates and peak temperatures attained within the W+Ti powder bed. Even with the smallest n_{TiC}/n_s , the temperature at the sample edge nearly reaches T_m Ti. A threefold increase of n_{TiC}/n_s raises the edge temperature by 1000 °C. The center is less sensitive; the interior temperature varies only by ~400 °C. Ideally, for best compaction results, the n_{TiC}/n_s should be adjusted such that as much as possible of the bulk of the alloy powder bed is near, but does not exceed the T_m Ti, and excessive overheating of the periphery is minimized. However, unless a sufficiently large n_{TiC}/n_s is used, the entire W+Ti sample will not become isothermal during the early part of the heating cycle. The n_{TiC}/n_s of ~6.0 satisfies both of these criteria.

Aside from a more sluggish rise in the interior of the powder bed, the Mo-Ti system exhibited the same temperature response as the W-Ti system (figure 7). Note that the delayed temperature rise of TC no. 3 occurs in the interior of Mo+Ti powder bed. Such differences in the rate of temperature change in the precursor powder bed are primarily influenced by kinetic factors such as the thermal diffusivity of the powder mixture. Because Mo has a lower thermal diffusivity than W (16), all other factors in the fixture being constant, the thermal diffusivity of the Mo+Ti mixture will also be less. With a lower thermal diffusivity, the rate of change of the temperature in the Mo+Ti bed would be expected to be more sluggish.

Precompaction temperatures were also measured in the scale-up fixture. The lateral dimension of the W-Ti alloy powder bed was scaled from 50 to 75 mm. Within the scale-up fixture, the dimensional scaling of the internal components was identical to that of the standard fixture. However, because of the larger diameter of the powder bed, all five thermocouples fit along a single radius. Figure 8 indicates the relative positions along the radius. The thermocouple data reveal that the peak temperatures are similar to those obtained previously. However, the rate of heating in the powder bed is proportionately slower and the position of the isothermal plateau is shifted from 60 to 140 s. The delay time does not scale linearly with the lateral fixture dimensions, but, rather, scales quadratically, i.e., with the volume. A peak temperature of 1800 °C was measured at the edge, with none of the interior temperatures exceeding 1500 °C. At the edge, the temperature rises to its maximum value, then declines gradually through the isothermal plateau. The rise in the interior is more moderate, monotonically reaching the isothermal plateau. Beyond the plateau region, the powder bed slowly cools to ambient temperature.

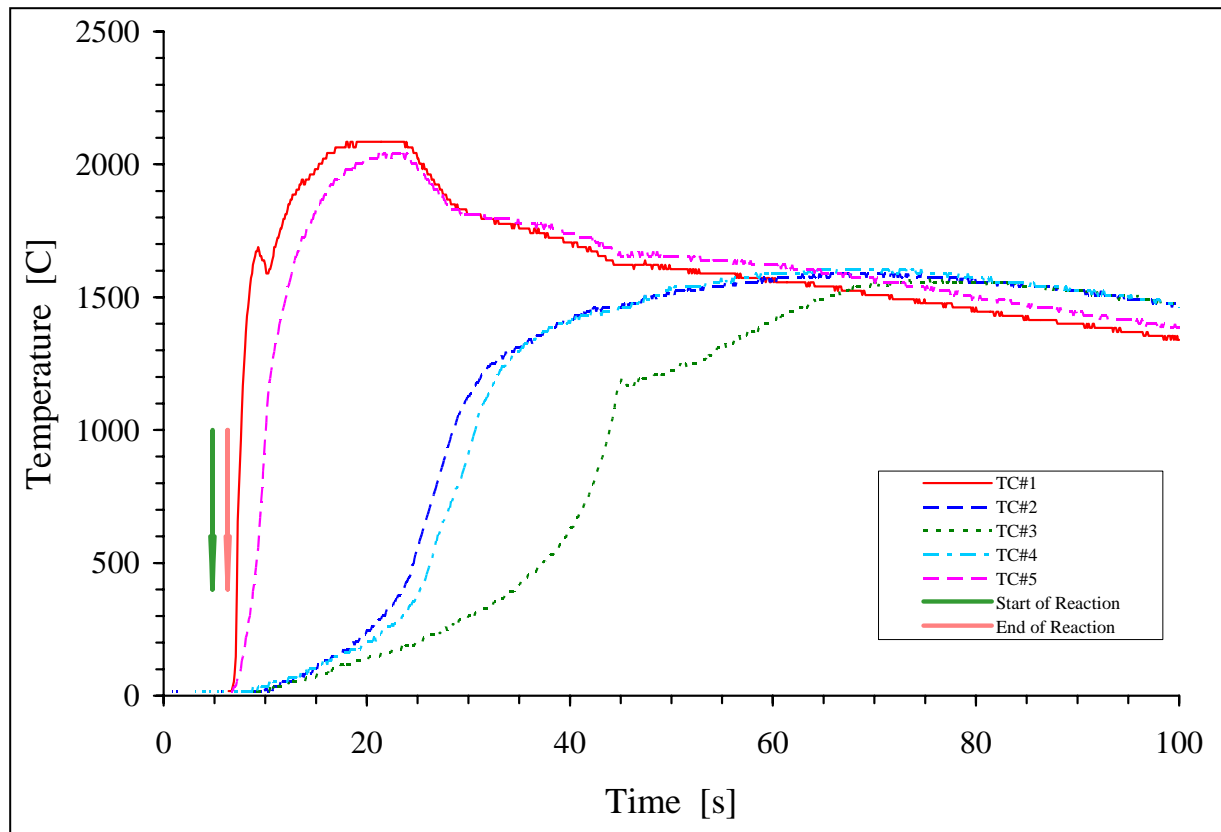


Figure 7. Temperature data for Mo–Ti; $n_{\text{TiC}}/n_s = 5.8$.

The extended delay time alters the relative ease of operations of the HEC process. Primarily, to protect the explosives from overheating or melting. The longer delay times needed to reach the isothermal condition will require a remotely operable explosive handling and transfer system, much like that used by Gorobtsov and Roman (3). More importantly, as illustrated with the increase from 50- to 75-mm-diameter billets, further lateral scaling with much longer delay times will dictate an alternative method of encapsulation of the sample to prevent exposure to air or other contamination.

3.2 Compaction Characteristics

During compaction of the contents of the HEC fixture, two main factors had to be considered. These were the yield strengths of the internal components and their respective temperature histories prior to compaction. From the bowed cross-sectional appearance of components, corresponding to nonuniform deformation, it was deduced that the compressive wave was not entirely planar (i.e., uniaxial) during compaction (17). Additionally, from the shape of the deformed alloy billet near its edges, it was inferred that the compaction pressure was at least comparable to, if not higher than, the high-temperature yield strengths of β -Ti and W or Mo.

Differences in yield strengths of the piston, steel anvils, ZrO_2 , TiC, and the W–Ti billet resulted in a limited, radially inward deformation of the more plastic components at the expense of others. Only the local distortion of the TiC and ZrO_2 disks, in direct contact with the sample powder bed, had a marked effect on the shape of the compacted alloy billet.

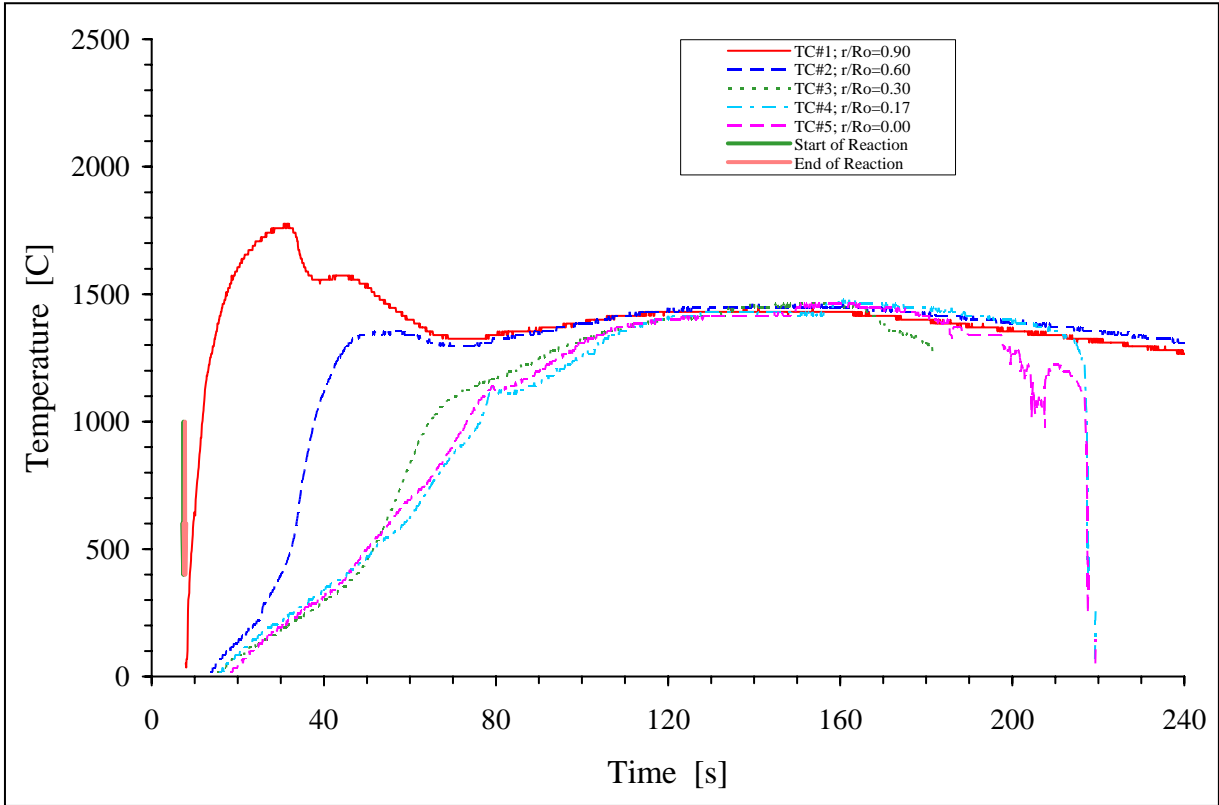


Figure 8. Temperature data for W–Ti in the scaled-up fixture; $n_{\text{TiC}}/n_s = 6.0$.

The ZrO_2 disk above the sample powder bed remained relatively cool. Therefore, it did not entirely sinter after consolidation. The upper one-third of the disk disintegrated into a fine powder; the lower two-thirds of the disk was sintered but with crazing cracks. Because of excessive overheating by the TiC reaction during and after consolidation, the ZrO_2 disk below the powder bed was more sintered and contained fewer cracks, but its outer periphery was completely eroded.

The recovered TiC doughnut was highly friable and was usually compacted to about 90% theoretical density (TD) only. However, at the time of consolidation, the doughnut was sufficiently plastic to deform, filling the fixture cavity. Its outer wall was straight, matching the contour of the fixture; its inner wall was irregular, matching the contour of the inner core (consisting of the anvils, ZrO_2 disks, and sample billet). The TiC formed an annular shear lip below the billet, partially filling the space vacated by the eroded lower ZrO_2 disk. This flow was incomplete, and a slight gap remained between the smaller ZrO_2 disk and the TiC lip. The gap was filled by the collapsing sample powder bed (18) upon consolidation.

The disk-shaped HEC billets were ~9 mm thick with a diameter of 50 mm. Figure 9 presents a macrophotograph showing the top, bottom, and side views of a typical W–Ti billet. The cut halves of the disk are placed with their bottom surfaces facing inward to form the side view. The top surface of the billet is mostly flat, while the bottom surface is slightly convex with a ridge forming at its edge. This small ridge is about 6.4 mm wide and 3.2 mm high and readily fractures off. The texture of the billet's side ranges from very fine to coarse striations and creases.

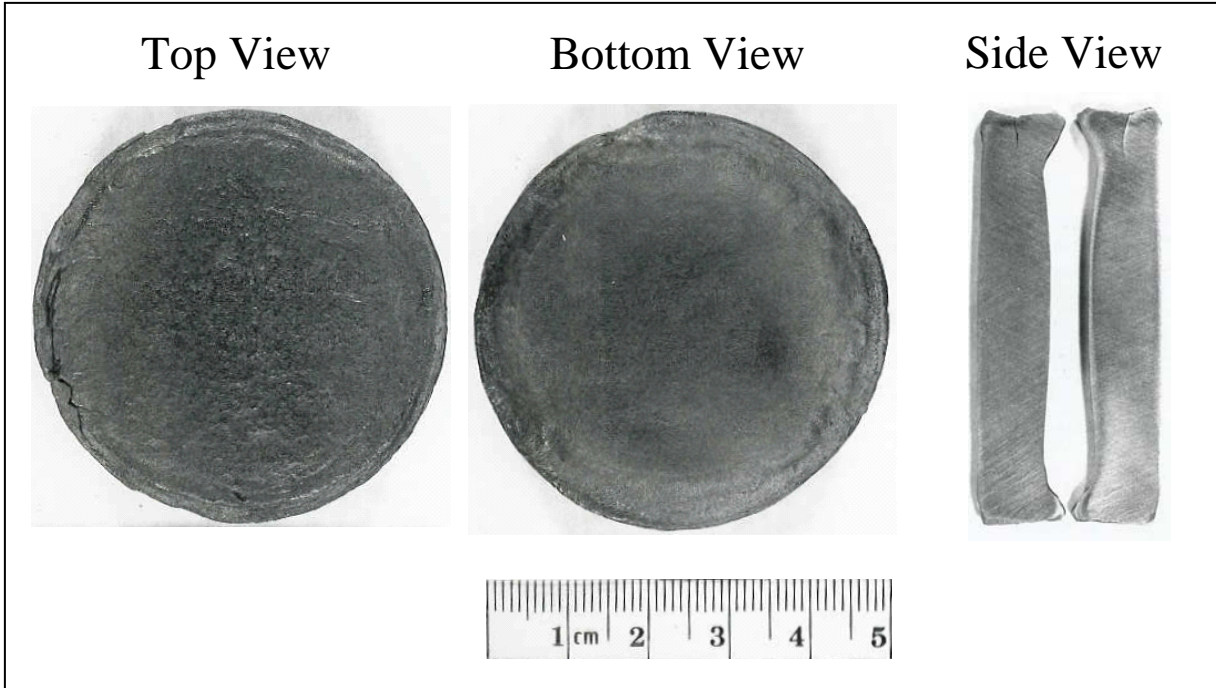


Figure 9. Macrophotographs of a typical W–Ti billet showing top, bottom, and side views (sectioned billet placed bottom to bottom).

The billets could be divided into an inner core and a periphery. Typically, the core comprised a disk with a diameter of ~35–40 mm, while the periphery comprised the outer 10- to 15-mm annulus of the billet. The periphery could be further divided into a 5-mm-wide outer edge and an intermediate transitional region. The edge usually contained minor annular and radial cracks. No evidence of horizontal hairline cracks was found in the core of the billets. Occasionally, some of the cores contained a random network of vertical hairline cracks. After sectioning such cores, the cracks were seen to occur along diagonals, originating at the top or bottom billet surface and terminating at the sides. Most likely, these cracks were caused by the reflection of the compressive wave from the free surfaces of the fixture during consolidation.

Results of the experiments with varying n_{TiC}/n_s indicated that the density of W–Ti decreases with n_{TiC}/n_s . A density of 99.1% TD was achieved at $n_{TiC}/n_s = 3.2$, while a density of 98.6% TD was obtained with $n_{TiC}/n_s = 6.4$. Lastly, a density of only 96.3% TD was reached for $n_{TiC}/n_s = 8.3$. It is speculated that, during consolidation at higher n_{TiC}/n_s values, the outer zone of the sample becomes more plastic, causing exit routes to be closed, thereby trapping the interior porosity. As expected, due to the lower T_m of Mo and greater thermal softening, densification was better for the Mo–Ti sample; specifically, a density of 99.1% TD was obtained using $n_{TiC}/n_s = 5.8$.

In a preliminary attempt to examine the feasibility of scale up, the standard weldings that held the fixture parts together failed during detonation, causing the loss of containment. The W–Ti billet was fully dense (98.2% TD) but was recovered in several fragments. For the second attempt, the welds were reinforced and strengthened to avoid detonation damage. This test resulted in a whole

disk-shaped billet that was fully dense (99.1% TD), with a slightly convex bottom surface. While successful, primarily because of weight, size, and heating time limitations, further lateral scaling of the HEC fixture will necessitate the use of machine-operated assembly, delivery, and recovery operations.

3.3 Alloy Substructures

SEM of the W powder revealed polyhedral particles, with a coarse surface texture, ranging in size from 5 to 20 μm . The Mo was polyhedral and faceted, ranging in size from 10 to 30 μm . The Ti was irregular, having faceted to elongated shapes, with a size range of 10–40 μm .

Baseline XRD measurements of the precursor powder lattice parameters were in agreement with nominal values for Mo, W, and Ti. XRD scans in figures 10 and 11 show that the cores of the alloys have a two-phase structure. In figure 10 for W–Ti with $n_{\text{TiC}}/n_s = 6.4$, the W diffraction peaks are clearly seen. Likewise, in figure 11 for Mo–Ti with $n_{\text{TiC}}/n_s = 5.8$, the diffraction peaks for Mo are easily identified. A second phase in each alloy appears as a shoulder (with an inflection point) on the low-angle side of each main peak. In Mo–Ti, the shoulders are more magnified and much wider, extending to lower angles. Unlike W–Ti, a few distinct peaks also appear on the shoulders.

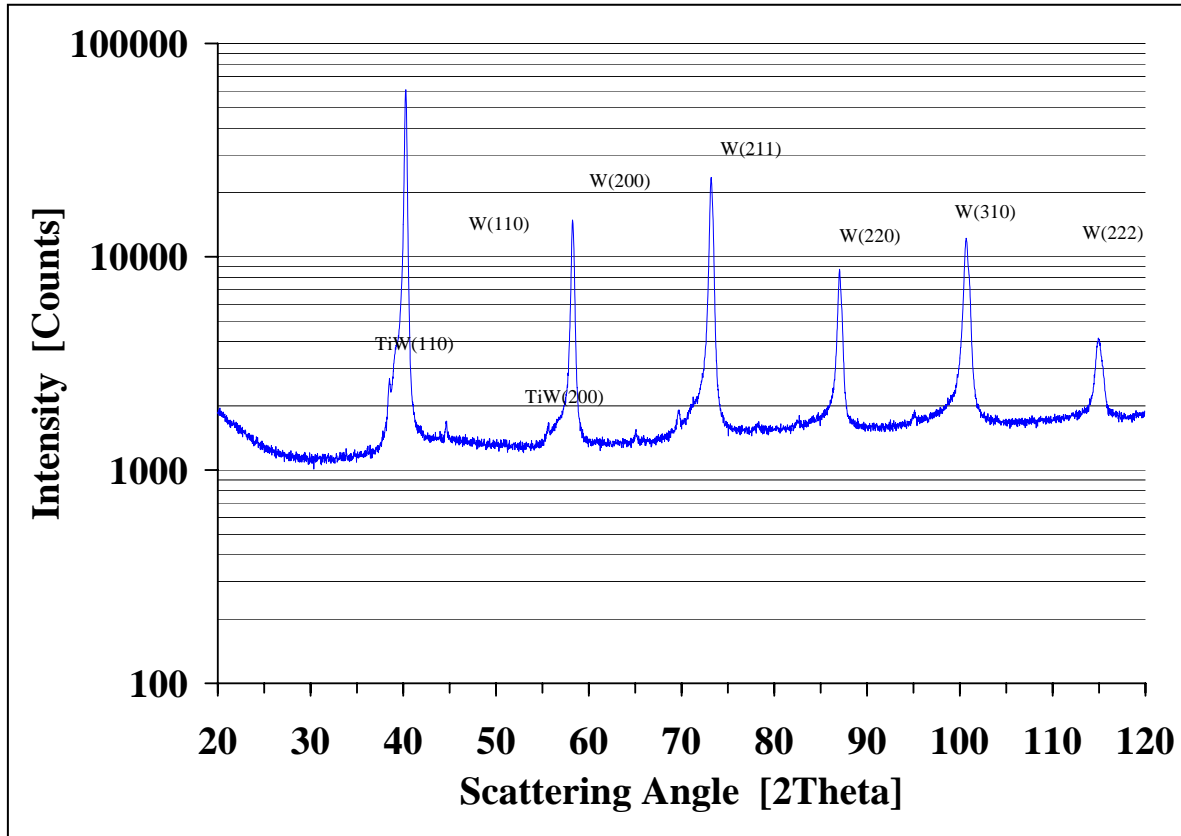


Figure 10. XRD scans of typical HEC billet core regions; W–Ti is shown in 7A and Mo–Ti is shown in 7B.

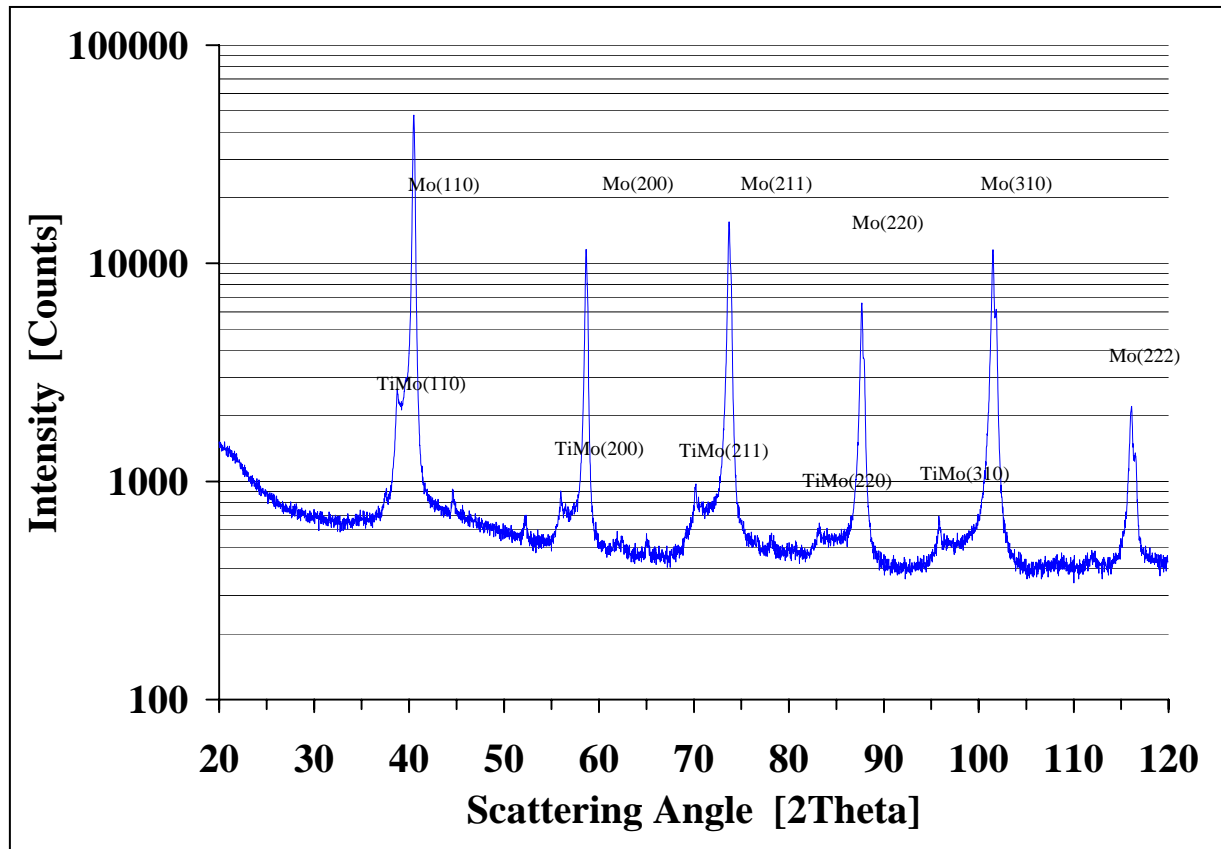


Figure 11. XRD scans of typical HEC billet core regions; W Ti is shown in 7A and Mo Ti is shown in 7B.

SEM of transverse (perpendicular) and longitudinal (parallel) cross sections (with respect to the compaction axis) revealed a preferentially oriented two-phase structure. The distribution of the primary and secondary phases is isotropic in the transverse section; however, both phases tend to be elongated along a transverse plane in the longitudinal section. Consistent with compaction wherein grains deform plastically without exceeding the breaking stress in the powder body, this orientation effect arose from the uniaxial collapse of the initially isotropic powder bed.

Figure 12 illustrates typical axial cross sections from the alloy core regions. W–Ti with $n_{TiC}/n_s = 6.4$ is shown in figure 12, and Mo–Ti with $n_{TiC}/n_s = 5.8$ is shown in figure 12.

Observation of the W–Ti core reveals loose W grain aggregates (light gray) bounded by a partially connected Ti-rich matrix (dark gray). The partial discontinuity of the matrix comes from the particle size difference of the precursors, the relative melting points, and the temperature before and at the time of compaction. The W grains have retained their original size of 10–20 μm . The dimensions of the Ti-rich areas, likewise, correspond to the size of the Ti precursor. EDS indicates that the W in the aggregates is nearly pure and the fairly uniform Ti-rich phase has a composition of ~25W–75Ti a/o. The second phase observed in the XRD measurements is this Ti-rich β –Ti/W solid solution (19).

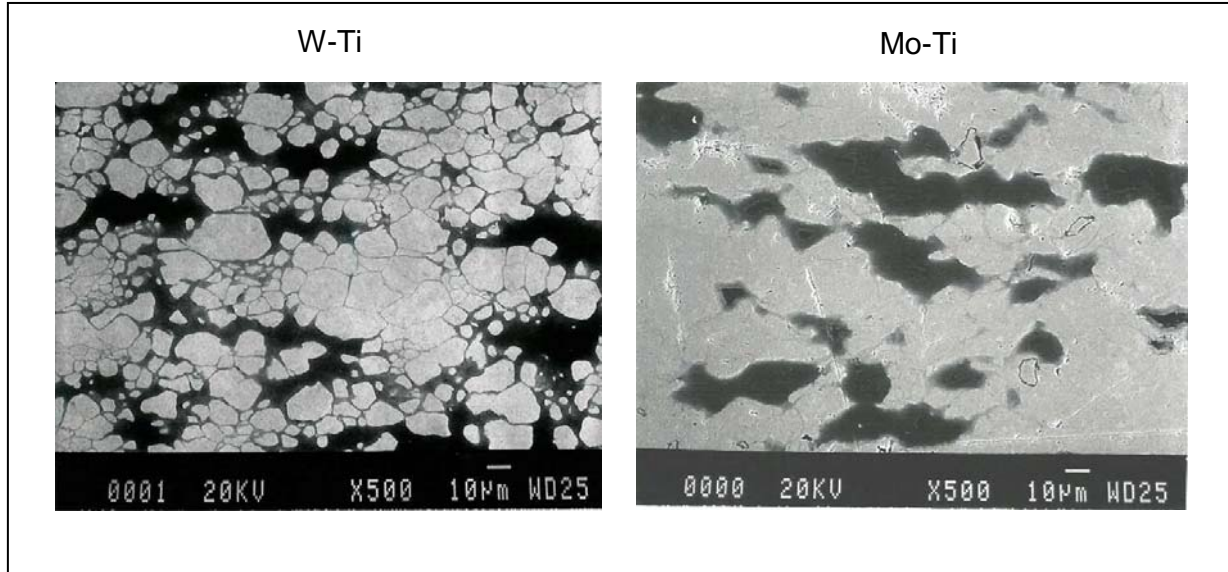


Figure 12. SEMs of polished surfaces of typical HEC billet core regions; W-Ti is shown in 8A and Mo-Ti is shown in 8B.

Unlike W-Ti, the Mo grain aggregates (light gray) in the Mo-Ti alloy are more interconnected, surrounding mostly isolated Ti-rich matrix regions (medium to dark gray). The Mo grains have a size of 10–30 μm . The dimensions of the Ti-rich matrix regions correspond to those of the Ti precursor. EDS indicates that the Mo in the aggregates is mostly pure. As evident in the figure, the Ti-rich matrix phase is segregated and nonuniform. The composition of the medium-gray areas ranges from 25Mo–75Ti to 15Mo–85Ti a/o. In contrast, the composition of the dark-gray areas is mostly pure Ti. The low-angle shoulders, noted in the XRD scans, correspond to the Ti-rich β -Ti/Mo solid solution (19). The increased width and height of the shoulders support the observed compositional nonuniformity. Finally, some of the distinct shoulder peaks at 20 of 34.9, 38.7, 52.2, 63, and 70.1° are probably associated with the mostly pure Ti regions.

The presence of the secondary matrix phase obscures the evolution of the alloy microstructures. The added complexity derives from the intermixing of the constituents at elevated temperatures. In the W-Ti alloy, because of the moderately fast diffusion of W in Ti (20) and the fact that the sample is consolidated after a sufficiently long time delay, it was expected that the composition of the β -Ti/W solid solution would equilibrate during heating. That is, the concentration gradient introduced by a solid-state dissolution of the W grain outer layers in Ti would be quickly reduced by fast diffusion. In the absence of a composition gradient (i.e., that introduced by slow diffusion), the rate-controlling step of the process is the dissolution of W during heating. The relative compositional uniformity of the matrix in the W-Ti alloy core is in agreement with this assessment.

Within the context of the HEC system thermodynamics, the Mo-Ti matrix ought to be compositionally uniform similar to that found in the W-Ti alloy. However, despite of a higher diffusion rate of Mo in Ti (about three times than that of W in Ti) and the strong similarities

between the Mo–Ti and W–Ti phase diagrams (19), the Mo–Ti matrix composition is not uniform. Due to the lower thermal diffusivity of Mo, the 60-s compaction delay time is most likely insufficient to allow adequate equilibration of the β –Ti/Mo matrix. The more sluggish temperature rise reduces the effectiveness of heating, and a shorter time at temperature, in turn, prevents the homogenization of the matrix.

4. Conclusions

A technique whereby high-density, monolithic, single- or multi-phase alloy billets can be fabricated has been demonstrated. HEC was conceived primarily for use with difficult-to-consolidate refractory alloys when conventional methods are not applicable. In this technique, the precursors are first heated by an external exothermic combustion synthesis reaction. When such a reaction takes place in a properly insulated fixture, the powdered precursors can be quickly heated to very high temperatures. Compaction to full density is accomplished by the pressure wave generated during the detonation of an explosive. The thermal diffusion length of the heating heat pulse only limits the lateral dimensions of the billets.

The fundamental appeal of this technique hinges on the shortened processing cycles that are characteristic of this process. Concurrent with the application of dynamic pressures, rapid heating and cooling permit the formation and retention of nonequilibrium structures that are otherwise unobtainable with conventional forming methods. It was shown with W–Ti and Mo–Ti alloys that adjustment of the heating rate and peak temperature during heating, as well as the thermal management of heat losses upon cooling, could affect the compositional intermixing and heterogeneity within the sample billets.

The W–Ti alloy billet core is of high density and has a two-phase structure of W particles embedded in a partially continuous Ti-rich β –Ti/W solid-solution matrix. Experiments with the Mo–Ti system resulted in similar overall alloy characteristics. Within the interior, unlike the matrix in W–Ti, the matrix in Mo–Ti is nonuniform. This nonuniformity arises from the sluggish kinetics of the heating phase, causing the dissolution of Mo to be incomplete. Phase uniformity may be improved by HEC fixture modifications to increase the amount of ZrO_2 insulation or the type of chemical furnace material such that the duration of the isothermal plateau is lengthened.

5. References

1. Linse, V. D. Dynamic Compaction of Metal and Ceramic Powders. *Sagamore Army Material Research Conference. Innovation in Materials Processing*; Bruggeman, G., Weiss, V., Eds.; Plenum Press: New York, NY, **1983**, 30, 381–404.
2. Cross, A. *Try Hot Explosive-Compacting for Sintered Powder Products*. *Iron Age* **1959**, 184 (26), 48–50.
3. Gorobtsov, V. G.; Roman, O. V. Hot Explosive Pressing of Powders. *International Journal of Powder Metall. and Powder Tech.* **1975**, 11 (1), 55–60.
4. Wang, S. L.; Meyers, M. A.; Szeket, A. Warm Shock Consolidation of IN 718 Powder. *Journal of Material Science* **1988**, 23 (5), 1786–1804.
5. Ferreira, A.; Meyers, M. A.; Thadhani, N. N.; Chang, S. N.; Kough, J. R. Dynamic Compaction of Titanium Aluminides by Explosively Generated Shock Waves: Experimental and Materials Systems. *Metall. Trans. A* **1991**, 22 (3), 685–695.
6. Taniguchi, T.; Kondo, K. Hot Shock Compaction of α -Alumina Powder. *Adv. of Ceramic Materials* **1988**, 3 (4), 399–402.
7. Yoshida, M.; Yoshioka, Y.; Kimura, Y.; Hirabayashi, H.; Sawaoka, A. B.; Pruemmer, R. A. Explosive Hot Consolidation of Alumina Powder. Influence on Structure. *Aerospace, Refractory and Advanced Materials Advances in Powder Metallurgy*; Metal Powder Industries Federation: Princeton, NJ, 1991, no. 6, pp 199–209.
8. Shang, S. S.; Hokamoto, K.; Meyers, M. A. Hot Dynamic Consolidation of Hard Ceramics. *Journal of Material Science* **1992**, 27 (20), 5470–5476.
9. Peikrishvili, A.; Japaridze, L.; Chikhradze, N.; Chagelishvili, E. Possibilities of Obtaining Combined Samples from Tungsten-Based Alloys by High-Temperature Shock Wave Treatment. *Metallurgical and Materials Applications of Shock-Wave and High-Strain-Rate Phenomena*; Murr, L. E., Staudhammer, K. P., Meyers, M. A., Eds., Elsevier: Amsterdam, The Netherlands, 1995, chap. 14, pp 99–108.
10. Kecskes, L. J.; Hall, I. W. *Hot Explosive Consolidation of W–Ti Alloys*. ARL-TR-669; U.S. Army Research Laboratory: Aberdeen Proving Ground, MD, 1995.
11. Rhinehart, J. S.; Pearson, J. *Explosive Working of Metals*; MacMillan Company: New York, NY, 1963; chap. 9, p 257.
12. Akashi, T; Sawaoka, A. B. High Density Compacts. U.S. Patent 4,655,830, 1987.

13. Munir, Z. A. Synthesis of High-Temperature Materials by Self-Propagating Combustion Methods. *Ceramics Bulletin* **1988**, 67 (2), 342–349.
14. *Materials Processing by Self-Propagating High-Temperature Synthesis (SHS)*. DARPA/ARMY SHS Symposium Proceedings, MTL-SP-87-3, Gabriel, K. A., Wax, S. G., McCauley, J. W., Eds.; U.S. Government Printing Office: Washington, DC, 1985.
15. *Combustion and Plasma Synthesis of High-Temperature Materials*. Munir, Z. A., Holt, J. B., Eds.; VCH Publishers, Inc.: New York, NY, 1990.
16. *Handbook of Chemistry and Physics*. Weast, R. C., Ed.; Chemical Rubber Company Press: Cleveland, OH, 54th ed, 1973.
17. Gourdin, W. H. Dynamic Consolidation of Metal Powders. *Prog. Material Science* **1986**, 30 (1), 39–80.
18. Page, N. W.; Killen, P. D. Powder Flow During Dynamic and Quasistatic Compaction. *Powder Metal.* **1987**, 30 (4), 233–239.
19. *Binary Alloy Phase Diagrams*. Massalski, T. B., Okamoto, H., Subramanian, P. R., Kacprzak, L., Eds.; William W. Scott: New York, NY, 1990.
20. Askill, J. *Tracer Diffusion Data for Metals, Alloys, and Simple Oxides*; Plenum Data Corporation: New York, NY, 1970, pp 52–53.

<u>NO. OF COPIES</u>	<u>ORGANIZATION</u>	<u>NO. OF COPIES</u>	<u>ORGANIZATION</u>
1 (PDF ONLY)	DEFENSE TECHNICAL INFORMATION CTR DTIC OCA 8725 JOHN J KINGMAN RD STE 0944 FORT BELVOIR VA 22060-6218	1	<u>ABERDEEN PROVING GROUND</u> DIR USARL AMSRD ARL CI OK TP (BLDG 4600)
1	US ARMY RSRCH DEV & ENGRG CMD SYSTEMS OF SYSTEMS INTEGRATION AMSRD SS T 6000 6TH ST STE 100 FORT BELVOIR VA 22060-5608		
1	INST FOR ADVNCD TCHNLGY THE UNIV OF TEXAS AT AUSTIN 3925 W BRAKER LN STE 400 AUSTIN TX 78759-5316		
1	US MILITARY ACADEMY MATH SCI CTR EXCELLENCE MADN MATH THAYER HALL WEST POINT NY 10996-1786		
1	DIRECTOR US ARMY RESEARCH LAB IMNE ALC IMS 2800 POWDER MILL RD ADELPHI MD 20783-1197		
3	DIRECTOR US ARMY RESEARCH LAB AMSRD ARL CI OK TL 2800 POWDER MILL RD ADELPHI MD 20783-1197		
3	DIRECTOR US ARMY RESEARCH LAB AMSRD ARL CS IS T 2800 POWDER MILL RD ADELPHI MD 20783-1197		

NO. OF
COPIES ORGANIZATION

ABERDEEN PROVING GROUND

30 DIR USARL
AMSRD ARL WM MB
L KECSKES